remote sensing

MDPI

Article

Improving the Accuracy of Optical Satellite-Derived Bathymetry Through High Spatial, Spectral, and Temporal Resolutions

Giovanni Andrea Nocera [1,2], Valeria Lo Presti [3], Attilio Sulli [3] and Antonino Maltese [1,*]

[1] Dipartimento di Ingegneria, Università degli Studi di Palermo, Viale delle Scienze, Edificio 8, 90128 Palermo, Italy; giovanniandrea.nocera@unipa.it
[2] National Biodiversity Future Center (NBFC), Piazza Marina 61, 90133 Palermo, Italy
[3] Dipartimento di Scienze della Terra e del Mare, Università degli Studi di Palermo, Piazza Marina, 61, 90133 Palermo, Italy; valeria.lopresti@unipa.it (V.L.P.); attilio.sulli@unipa.it (A.S.)
* Correspondence: antonino.maltese@unipa.it

Highlights

What are the main findings?

- An integrated approach leveraging spectral and temporal averaging of PlanetScope SuperDove imagery enhances the accuracy of satellite-derived bathymetry in shallow coastal waters.
- The integration of liquid-facet-dependent noise reduction and depth-dependent diffuse attenuation coefficient further refines the model, reducing signal variability and improving depth estimation.

What are the implications of the main findings?

- The proposed approach can yield satellite-derived bathymetry with ±6% error up to 25 m depth.
- This technique enables cost-effective, high-resolution bathymetric mapping in nearshore zones where traditional surveys are limited or expensive.

Abstract

Accurate nearshore bathymetry is essential for various marine applications, including navigation, resource management, and the protection of coastal ecosystems and the services they provide. This study presents an approach to enhance the accuracy of bathymetric estimates derived from high-spatial- and high-temporal-resolution optical satellite imagery. The proposed technique is particularly suited for multispectral sensors that acquire spectral bands sequentially rather than simultaneously. PlanetScope SuperDove imagery was employed and validated against bathymetric data collected using a multibeam echosounder. The study area is the Gulf of Sciacca, located along the southwestern coast of Sicily in the Mediterranean Sea. Here, multibeam data were acquired along transects that are subparallel to the shoreline, covering depths ranging from approximately 7 m to 50 m. Satellite imagery was radiometrically and atmospherically corrected and then processed using a simplified radiative transfer transformation to generate a continuous bathymetric map extending over the entire gulf. The resulting satellite-derived bathymetry achieved reliable accuracy between approximately 5 m and 25 m depth. Beyond these limits, excessive signal attenuation for higher depths and increased water turbidity close to shore introduced significant uncertainties. The innovative aspect of this approach lies in the combined use of spectral averaging among the most water-penetrating bands, temporal averaging across multiple acquisitions, and a liquid-facets noise reduction technique. The integration of these multi-layer inputs led to improved accuracy compared to using single-date or single-band

Check for updates

Academic Editor: Chung-Ru Ho

Received: 22 November 2025
Revised: 24 December 2025
Accepted: 11 January 2026
Published: 14 January 2026

Copyright: © 2026 by the authors. Licensee MDPI, Basel, Switzerland. This article is an open access article distributed under the terms and conditions of the Creative Commons Attribution (CC BY) license.

imagery alone. Results show a strong correlation between the satellite-derived bathymetry and multibeam measurements over sandy substrates, with an estimated error of ±6% at a 95% confidence interval. Some discrepancies, however, were observed in the presence of mixed pixels (e.g., submerged vegetation or rocky substrates) or surface artifacts.

Keywords: satellite derived bathymetry; high resolution bathymetry; multibeam echosounder; optical data

1. Introduction

In the context of the pressing environmental crisis, acquiring high-resolution bathymetric data in nearshore areas is crucial for understanding seafloor characteristics and conducting comprehensive mapping, thereby enabling a more informed and efficient use of marine territories. Recent progress in remote sensing technology has significantly improved our ability to map and monitor underwater environments. Numerous global and local bathymetric measurement campaigns have been conducted, yet information gaps persist. The Seabed 2030 project, an initiative led by The Nippon Foundation and General Bathymetric Chart of the Oceans (GEBCO), whose goal is to map the global sea floor by 2030 [1], has increased the amount of seafloor mapped from just 6% in 2017 to nearly 25% by 2023, covering an additional 5.4 × 106 km^2 of the ocean floor in just 6 years [2]. The latest available GEBCO bathymetric dataset was released in August 2025 [3].

To map seafloors, several techniques are employed, each with specific advantages and limitations [4–6]. Up to now, there is a growing need to map nearshore areas, particularly the white ribbon zone [7,8], which refers to areas along the coast where there is a lack of data due to the difficulty of surveying these regions. These areas are typically too shallow for most bathymetric survey vessels to navigate safely. As a result, such areas are often uncharted on nautical maps, appearing as a blank white strip. Efforts to map these missing zones often involve using expensive technologies like airborne Light Detection and Ranging (LiDAR) or an Autonomous Underwater Vehicle (AUV) equipped with echosounders, which can fill in these gaps by providing accurate bathymetric data for shallow coastal areas [9,10].

Table 1 reports an overview of some remote sensing techniques for bathymetric estimation, ordered from lower to higher geometric resolution:

- Synthetic Aperture Radar (SAR) bathymetry derives seafloor features by analyzing the interaction of radar signals with surface wave patterns. It is advantageous for its global coverage, independence from daylight, and weather conditions, though it has low spatial resolution and is less precise for greater depths [11,12].
- Optical Satellite-Derived Bathymetry (hereinafter simply referred as, SDB) utilizes multispectral satellite imagery to estimate water depth, leveraging the relationship between reflectance and depth. This method is particularly suitable for shallow waters, up to approximately 30 m. It covers large areas at relatively low costs but can have low accuracy depending on water turbidity and bottom composition [13,14].
- LiDAR bathymetry employs laser scanning to measure depths, providing highly detailed seabed information, especially in shallow waters. LiDAR enables the retrieval of information from greater depths than passive systems, due to the higher energy of the artificial signal, which penetrates more deeply than solar radiation (up to 40 m). The primary limitations are the high costs and reduced effectiveness in turbid waters [15,16].

- A Multibeam Echosounder employs an array of sonar beams to generate 3D representations of the seafloor. It delivers precise, high-resolution data, making it particularly suitable for analyses of complex seafloor. However, the technique is expensive, limited to areas accessible by vessels, and less effective in highly turbid or very deep waters [17,18].
- Underwater photogrammetry involves utilizing high-resolution images obtained through an AUV or Remote-Operated underwater Vehicle (ROV) to create detailed 3D models of the ocean floor. This technique is ideal for shallow, clear waters, but has a limited spatial coverage and relatively high cost [19,20].

Table 1. Summary of some of the most applied remote sensing techniques/instruments used to derive bathymetry.

Technique	Spatial Resolution	Area Coverage	Depth Target	Applications	Key Pros	Disadvantages
Satellite Altimetry	km	Global	All depths	Deep oceans, analysis of tectonic structures such as oceanic ridges	Global coverage, study remote regions	Low spatial resolution, relies on gravity models
SAR Bathymetry	km-m	Global	Shallow to moderate | ~50 m |	Coastal mapping, monitoring morphological changes	Independence of daylight and weather	Limited resolution, affected by sea state and waves
Optical SDB	m	Coastal	Shallow waters | ~30 m |	Shallow water mapping, coastal management	Wide-area coverage at low cost, rapid surveys	Affected by turbidity, bottom composition and lighting conditions
LiDAR Bathymetry	m-cm	Coastal	Shallow waters | ~40 m |	Coastal mapping, navigation channel surveys	High resolution, rapid surveys	Less effective in turbid waters, needs specific platforms, high cost
Multibeam Echosounder	m-cm	Only Vessel Accessible	All depths with different precision	Detailed analysis of complex seafloor structures	High resolution and high accuracy	Reduced performance in turbid/deep waters, expensive
Underwater Photogrammetry	cm-mm	Local	Shallow waters | ~30 m |	Detailed mapping of marine habitats in controlled conditions	Very high details (3D surveys)	Limited coverage, requires clear water, very high cost

The choice of bathymetric measurement technique depends on factors such as the scale of the area, water depth, spatial resolution, required precision, and available budget. Understanding these methods' advantages and limitations is crucial for selecting the most appropriate for specific research and application needs. Moreover, the integration of data from different sources has opened new avenues to improve the accuracy and efficiency of sea bottom investigation, particularly in coastal areas where high-ground-resolution data are pivotal for resource management, coastal engineering, and biodiversity conservation [21,22]. Here, we test an optical–acoustic data integration framework employing both multibeam echosounder data and optical satellite images.

As previously mentioned, the white ribbon denotes the zone where high-resolution bathymetric data are absent due to intrinsic challenges in collecting depth measurements in shallow water environments. These constraints hinder the deployment of vessels and

conventional seafloor mapping tools, leading to the exploration of alternative approaches, ranging from the use of AUV/ROV to airborne LiDAR. Unfortunately, these tools face additional limitations, primarily related to high costs.

In recent years, the ICESat-2 satellite, equipped with the ATLAS (Advanced Topographic Laser Altimeter System) LiDAR sensor, has become a widely used tool for collecting altimetric data, including measurements beneath the water surface. Many pivotal studies leverage ICESat-2 data for calibrating and validating bathymetric inversion models [15,23,24], yet several limitations persist in white ribbon mapping [25]. One major constraint is the sparse spatial coverage; indeed, ATLAS delivers only six narrow parallel tracks per overpass, grouped into three beam pairs spaced by ~3.3 km across-track and about 90 m within each pair. Over a full repeat cycle, the satellite overpasses 1387 reference ground tracks within a 91-day period. This configuration leads to a sparse sampling density and creates substantial gaps between data points, causing certain areas to remain unsampled [26].

The Gulf of Sciacca constitutes a particularly challenging setting for optical-derived bathymetry because of the presence of a white ribbon zone marked by strongly variable water turbidity, driven by sediment resuspension, coastal hydrodynamics, and localized anthropogenic influences. Under these conditions, water optical properties display pronounced temporal variability that violates the assumptions underlying both single-date optical methods and episodic LiDAR surveys. Consequently, conventional bathymetric mapping techniques frequently produce unstable or biased depth estimates in this region. Furthermore, considering the spatial constraints of the study area, which limit the availability of ICESat-2 tracks and sample points, multibeam echosounder data were employed to overcome biases in calibration and validation, thus focusing on the image processing pipeline.

The proposed framework (Figure 1) does not introduce a new bathymetric inversion model, but instead focuses on a robust integration strategy designed to stabilize SDB performance under optically complex and temporally variable coastal environments.

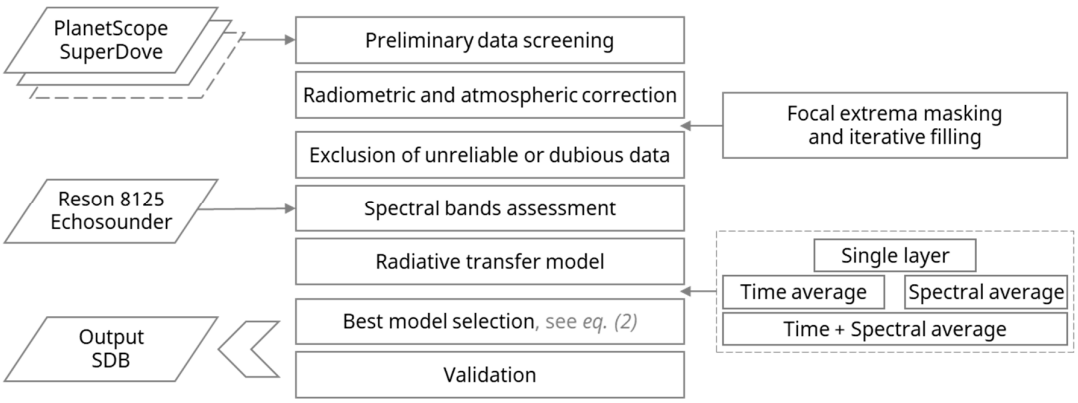


Figure 1. Research workflow: parallelograms indicate input and output data layers, while rectangles indicate methods applied. The dashed rectangular box includes all the steps of the averaging process.

Indeed, this study aims to demonstrate how the combination of various spectral bands and acquisition times from high-spatial/temporal-resolution satellite optical imagery enables the accurate reconstruction of nearshore bathymetry. Leveraging the extensive spatial coverage of satellite observations alongside the accuracy of acoustic measurements, the method represents a robust approach for bathymetric mapping in environments where traditional methodologies may face limitations.

2. Materials and Methods

The area under investigation is the nearshore of the Gulf of Sciacca, spanning from Capo San Marco (37.49°N; 13.02°E) promontory, on the south of the Carboj River mouth, to Capo Bianco (37.39°N; 13.27°E) promontory, close to the Platani River mouth, both on the southern coast of Sicily Island, Italy (Figure 2).

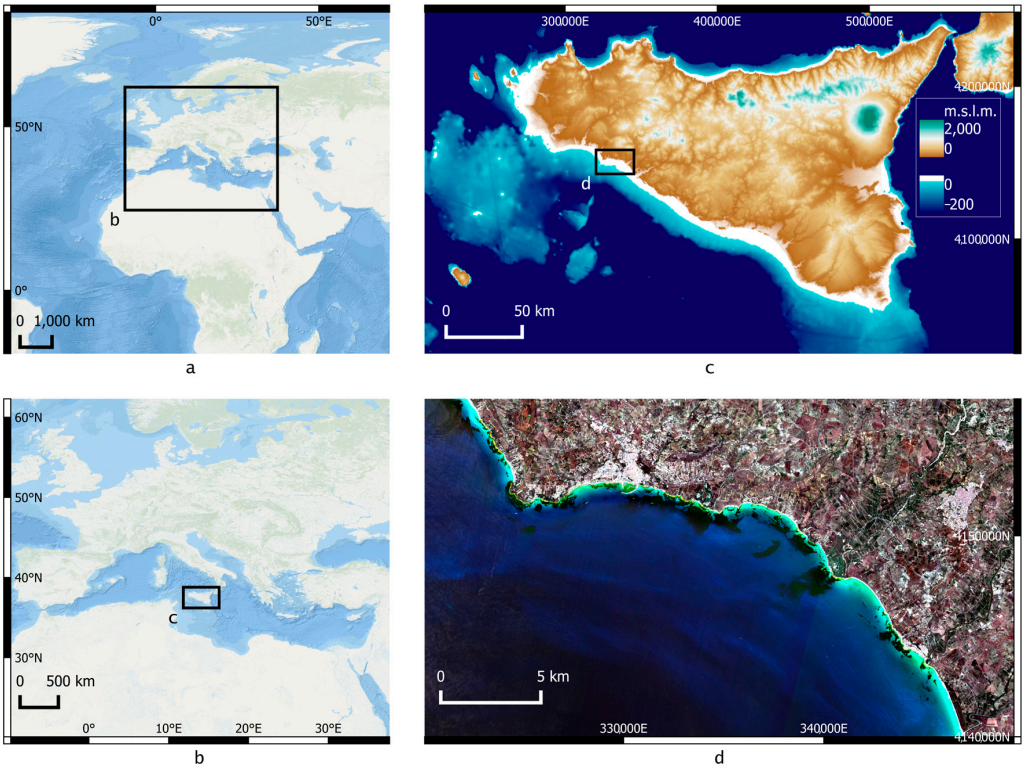


Figure 2. Location map of the study area. (**a**) Mediterranean basin. (**b**) Sicily Island in the Mediterranean Sea. (**c**) Altitude of Sicilian Island and bathymetry in the range of 2000 to −200 m over sea level; the water depths between 0 and 30 m are represented in white to highlight the extent to which the proposed method can be applied based on GEBCO 2024 data. (**d**) Focus on the Gulf of Sciacca; Sentinel 2 true color composite. Projected coordinate system (EPSG:7792) based on the RDN2008 datum, aligned with ETRS89, using the UTM projection in zone 33N.

From a geological point of view, the Gela Thrust Front (GTF) represents a major structural boundary, following a north–south direction approximately in correspondence of Verdura River. This geological formation divides, to the west, the Sicilian–Maghrebian Chain, and to the east, the Gela Formation [27,28]. The Sciacca offshore area is characterized as a subsiding basin with a northwest-southeast orientation, covered by over 2000 m of terrigenous or carbonate deposits. It forms part of the Plio-Pleistocene foredeep, situated near the "Gela nappe".

From a geomorphological perspective, the emerged territory is characterized by a hilly/mountainous landscape, with two large plateaus corresponding to the areas of Capo San Marco and Ribera. The lithological nature of the outcropping rocks and the presence of numerous rivers facilitate the availability of large quantities of sediments transported from the emerged sector towards the coast, forming elongated coastal plains. This continuous sedimentary process has shaped the marine sector throughout the Quaternary, resulting in a predominantly gentle morphology with minimal slope variations. Consequently, as shown in Figure 2c, in the investigated area the white ribbon extends over a broader area compared to regions with steeper bathymetric gradients. The upper boundary of the study

area is demarcated by the shoreline, representing the interface between terrestrial and marine environments.

Multibeam bathymetric surveys were conducted over 16 acquisition days between 3 February and 25 May 2023, utilizing a Reson SeaBat 8125 multibeam echosounder (by Teledyne RESON Inc., Thousand Oaks, CA, USA), characterized by an along-track transmit beam width of 1.0°, an across-track receive beam width of 0.5° at nadir, a maximum ping rate of 40 Hz, a pulse length of 10 µs to 300 µs, and a depth resolution of 6 mm.

The absolute accuracy of the bathymetric data is further influenced by operational conditions, including positioning accuracy during navigation, motion corrections (roll, pitch, heave), sound-velocity profiles, and the processing of the raw data. The dataset was processed with PDS2000 software (version 4.4.11.5), undergoing error removal and spatial interpolation to ensure a seamless grid, with no gaps. Interpolation methods were used to achieve the final DTM at a 0.5 m footprint resolution (Figure 3). Finally, the multibeam data were resampled from 0.5 m to 3 m using a spatial-average resampling method to serve as calibration for the satellite optical data, thereby mitigating potential misalignments between the multibeam and optical datasets.

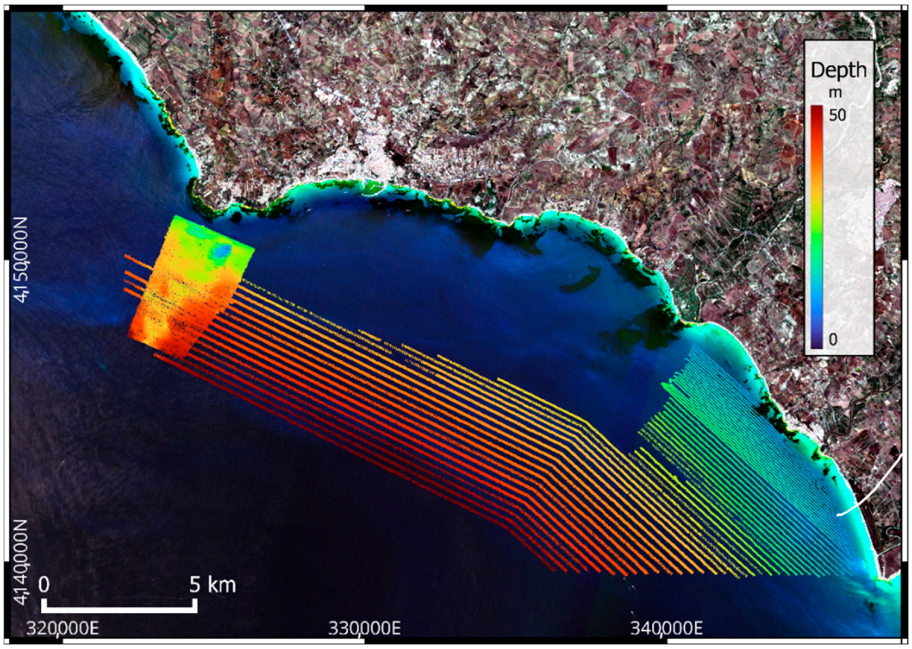


Figure 3. Pseudo color representation of the multibeam measured bathymetry. Data were collected on different dates: one dataset corresponds to a continuous survey of a small coastal promontory, whereas the other comprises multiple linear transects covering a wider offshore area.

The surveys revealed seafloor features of the Sciacca offshore region, focusing on the continental shelf down to −90 m. The structural high near Capo San Marco extends from the coast in an NNE-SSW direction to depths of over −40 m, with its shoals approaching −10 m depth about 1 mile from the coast; it is the result of significant tectonic features extending in a northeast-southwest direction. These features cause deformation and uplift of the substrate and the Quaternary cover. Here we observe rocky substrates, contouritic deposits, pockmark and mound structures and dense meadows of *Posidonia oceanica* (L.) Delile extending beyond −30 m. Similarly, at the Verdura River mouth, another high with rocky substrates supported a dense seagrass meadow. The easternmost sector, extending to Capo Bianco, presented sedimentary structures (megaripples and dunes) and diverse rocky substrates supporting patches of *Cymodocea nodosa* (Ucria) Asch. and *Posidonia oceanica*. Just as in the emerging sector, the submerged sector is also affected by fluid seepage

from the seabed. The intense anthropogenic activity taking place offshore of Sciacca has been observed in multibeam data, especially in the marine area of Seccagrande. Here, numerous groups of boulders of different dimensions can be seen, aligning for over 3 km perpendicularly to the coastline, along with the presence of pyramid-shaped structures intended to act as deterrents against bottom trawling. The multibeam bathymetric data were acquired on separate dates. In one case, a small area near a coastal promontory was surveyed continuously, while in another case, the acquisition consisted of multiple linear stripes covering a broader offshore sector [29,30].

Optical data (i.e., satellite images) were acquired leveraging PlanetScope SuperDove satellite constellation, consisting of approximately 200 units, designed to provide daily global terrestrial imagery. This new generation of PlanetScope satellites, launched in early 2020, began producing imagery by mid-March of the same year and, by August 2021 provided a collection potential of 200 million km^2 per day. The constellation is incrementally deployed through a series of "flocks" of satellites, each conforming to the CubeSat 3U specification (10 cm × 10 cm × 30 cm) [31]. The newest generation of SuperDove is equipped with a PSBlue telescope (hereinafter, PSB.SD) (by Planet Labs PBC, San Francisco, CA, USA), with a 47-megapixel sensor, which provides high spatial (3 m) and spectral resolution (see Table 2), acquiring images using a butcher block filter. From 29 April 2022, all new PlanetScope images feature 8-bands and originate from PSB.SD. On-orbit performance is continually augmented through rapid integration of technological upgrades, enhancing both functional capacity and satellite count [32].

Table 2. PlanetScope SuperDove satellites, equipped with PSBlue telescope (PSB.SD), enable the acquisition of eight-spectral-band images.

Wavelength (nm)	B1 Coastal Blue	B2 Blue	B3 Green_I	B4 Green	B5 Yellow	B6 Red	B7 Red Edge	B8 NIR
Central	443	490	531	565	610	665	705	865
Range	431–452	465–515	513–549	547–583	600–620	650–680	697–713	845–885

Traditional multispectral sensors typically acquire four spectral bands spanning the visible and NIR regions, while PSB.SD sensors capture eight distinct segments of electromagnetic radiation. These eight bands feature different wavelength ranges: Bands 1 and 5 have the narrowest nominal acquisition range of ~20 nm, Bands 3, 4, 6, 7, and 8 fall within an intermediate range of 30–40 nm, while Band 2 has the widest nominal acquisition range, reaching 50 nm. Each frame consists of eight stripes, and to generate the final 8-band image, the consecutive frames on either side of a given frame are stacked together [33].

An important feature that proves advantageous for the technique developed in this study is that the spectral bands are not acquired simultaneously but sequentially, with a slight temporal offset between them. Given that the final scenes are reconstructed through a holographic processing of individual frames stitching up four frames ahead and four frames behind a reference frame [34], and that this reconstruction is performed separately and independently for each spectral band, it may lead to band-specific spatial discrepancies. In particular, the location of the most reflective pixels may differ across spectral layers due to the independent alignment and temporal offset inherent in the band-wise processing workflow. For instance, Aati et al. (2022) [34] report misalignment between the visible bands of the order of ~1 pixel.

According to Planet Labs [35], PlanetScope imagery products provided as Ortho Scenes undergo geometric corrections in which spacecraft-related effects are compensated using attitude telemetry and the best available ephemeris data and further refined through ground control points. This processing yields a positional accuracy of less than 10 m

RMSE at the 90th percentile. The Ground Sample Distance depends on satellite altitude and, for PSB.SD sensors range between 3.7 and 4.2 m. The imagery is resampled using a cubic-convolution kernel, resulting in an orthorectified pixel size of 3.0 m.

2.1. Preliminary Data Screening

The selection of satellite imagery for this investigation was driven by a series of predefined requirements. Through the Planet Explorer resource portal, search filters were applied to identify all cloud-free (0%) images acquired in 2022–2023 (i.e., temporally close to the multibeam echosounder survey), fully encompassing the study area. Subsequently, all images that visually exhibited high water turbidity, significant surface roughness caused by ocean waves, wind effects, or cloud shadows (Figure 4) were excluded. This filtering procedure was supported by quantitative metrics extracted directly from the imagery. Scenes characterized by unusually high mean reflectance in water-only pixels within the blue-green bands were identified as highly turbid, whereas images exhibiting pronounced fine-scale reflectance variability were interpreted as being affected by enhanced surface roughness induced by wind or wave activity. These metrics served as an objective validation of the visual screening. These conditions were essential in ensuring clear reflectance data, crucial for accurate bathymetric estimation.

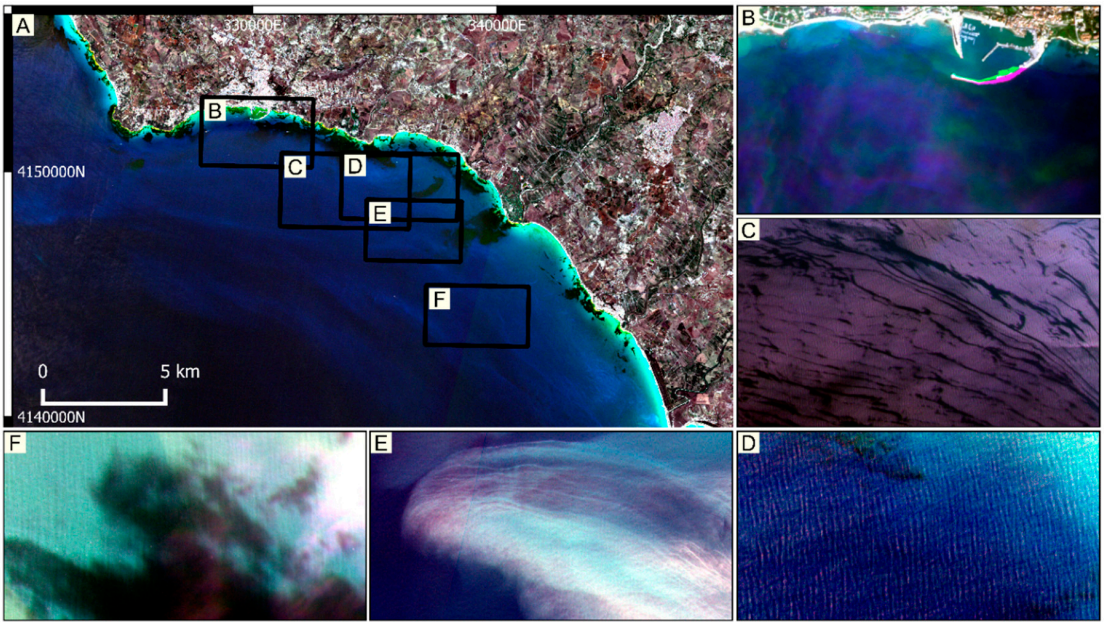


Figure 4. Representative examples of image quality issues that lead to exclusion during the refinement of the optical dataset. In particular, (**A**) shows the area under investigation, (**B**) refers to the presence of atmospheric dust inside the scene; (**C**) shows the combined effect of wind and marine water current; (**D**) exhibits surface roughness due to the presence of capillary waves; (**E**) shows the presence of dissolved materials in suspension; (**F**) refers to the issue of cloud shadows, from clouds beyond the scene boundaries, bypassing the cloud cover filter.

2.2. Radiometric and Atmospheric Correction

Radiometric data were calibrated to obtain Top of Atmosphere reflectance (ρ_{TOA}). A relative scatter algorithm, originally introduced by Chavez [36], was employed to perform atmospheric corrections. The refined Bottom of Atmosphere reflectance (ρ_{BOA}) was further adjusted with an empirical coefficient of 0.545 [37] to enhance the accuracy of sub-surface reflectance estimates.

2.3. Shoreline Extraction

The shoreline was extracted according to the Isoradiometric method [38,39] by processing the selected satellite images. The approach was first proposed by the authors [40] to detect shorelines by identifying abrupt radiometric transitions in remote sensing imagery. Here, it was applied as it provides an accurate and computationally efficient approach to derive the bathymetry upper boundary (depth equals 0 m) for calibrating the radiative transfer equation (see Section 2, Equation (1)).

2.4. Exclusion of Unreliable or Dubious Data

To obtain a reflectance dataset suited for bathymetric model calibration, we restricted our analysis to a single class of sandy seabed. More specifically, vegetated and rocky substrates were eliminated, retaining only the sandy seafloor, which exhibits characteristically higher reflectance. This was accomplished using a k-means clustering algorithm to classify the seafloor, and only the sandy class was retained as the optical input for our dataset. This classification was based on the research team's geological knowledge of the study area. However, the classes were finally assigned through visual interpretation and discrimination. The NIR band was employed to identify and exclude surface artifacts such as vessels, wake patterns, and other surface perturbations, ensuring a more refined dataset.

2.5. Spectral Bands Assessment

The diffuse attenuation coefficient (K_d) in aquatic environments governs the extent to which light is absorbed and scattered as it travels through the water column. This attenuation varies notably across the electromagnetic spectrum due to the optical properties of water and its components, including phytoplankton, suspended sediments, and dissolved organic matter (DOM) [41–43]. In the visible region of the spectrum, light attenuation in water is highly wavelength-dependent, with shorter wavelengths exhibiting higher penetrability compared to longer ones. This differential penetration is due to the relatively lower absorption and higher scattering of blue and green light due to the width of their characteristic wavelengths. In contrast, the red band and, even more, the NIR band suffer from rapid attenuation in water, limiting their use in subsurface observations. In particular, water strongly absorbs NIR radiation, meaning that NIR reflectance typically reports information about surface properties or the presence of floating materials. Based on these considerations, the K_d was carefully evaluated for each band and were selected those that maximize penetrability and minimize attenuation.

2.6. Spectral Average

The effectiveness of using individual spectral bands versus the average of two or more bands was analyzed. As widely documented in the scientific literature, the most effective and commonly employed optical wavelengths for bathymetric detection in coastal waters are in the range 490–565 nm, corresponding, respectively, to blue-green light [16]. Given the identification of the most penetrating wavelengths in the water column, we averaged the reflectance values of two or more informational layers corresponding to different spectral bands and carried out experimental analyses using these newly generated spectral mean layers. These preliminary outcomes are illustrated in Section 3.

2.7. Time Average

After identifying the most suitable images for bathymetric retrieval, temporal averaging was investigated by comparing the bathymetry estimated from single image acquisition with that derived from the average of two or more images. This was implemented to enhance data stability and minimize the influence of single-scene perturbations. The ef-

fectiveness of this approach varies depending on acquisition conditions. Outcomes are reported in Section 3.

2.8. Model Calibration

To ensure accurate calibration, the multibeam bathymetry (hereinafter MB) data layer was refined by removing all pixels associated with rocky or vegetated seabed. This more homogeneous dataset improved the consistency between reflectance values and bathymetry, thereby enhancing the accuracy of the correlation. Only pixels over sandy bottom have been used to calibrate the model. Subsequently, we applied a simplified version of the radiative transfer equation, originally proposed by Jain and Miller (1977) [44] in terms of radiance and later rephrased by Moussa et al. (1989) [45] in terms of reflectance, here linearized through a logarithmic transformation (1):

$$ln\left(\rho_0^\lambda - \rho_\infty^\lambda\right) = ln\left(\rho_b^\lambda - \rho_\infty^\lambda\right) - 2K_d^\lambda Z \quad (1)$$

where ρ_0^λ is the spectral reflectance just beneath the water's surface, ρ_∞^λ denotes the spectral reflectance value for a water column of infinite depth, ρ_b^λ is the spectral reflectance at the bottom, K_d^λ (m^{-1}) is the spectral diffuse attenuation coefficient, usually assumed as spatially constant, and Z (m) is the water depth. All parameters, except for depth, are wavelength-dependent [46].

To incorporate both spectral or/and temporal averaging we define the spectral–temporal average of the quantity ρ_0^λ as (2):

$$\langle \rho_0 \rangle = \frac{1}{TL} \sum_{t=1}^{T} \sum_{\lambda=1}^{L} \rho_0^\lambda(t) \quad (2)$$

where T is the number of temporal acquisitions and L is the number of spectral bands considered in the averaging. Although ρ_∞ , ρ_b , K_d can be estimated directly from the $\langle \rho_0 \rangle$ image, or via in situ radiometric measurements (e.g., K_d) they may also be calibrated when appropriate in situ reference data are available.

The corresponding expression considering spectral (λ) and temporal (t) average is given by (3):

$$ln(\langle \rho_0 \rangle - \rho_\infty) = ln(\rho_b - \rho_\infty) - 2K_d Z \quad (3)$$

Equation (3) was calibrated using a natural logarithm function fitting reflectance vs. MB. After calculating the coefficients of the logarithmic model, we used them to estimate the bathymetry from reflectance, producing an SDB of the whole area.

2.9. Validation

To ensure the accuracy of each SDB, we analyzed the relationship among 100,000 randomly sampled pixels selected from the MB dataset, considering depths down to 25 m, only on sandy bottom. The validation density plots (see Section 3) include a linear trendline along with two additional lines representing the 95th and 5th percentiles of SDB (Z_{op}) as a function of MB (Z_{mb}). Half the width of the confidence interval will be assumed as a metric for the dispersion relative to the trendline.

2.10. Reduction in Liquid-Facet-Dependent Noise

The radiative transfer process in marine environments is inherently complex and dynamic. Even when the direction of incident solar radiation and the satellite viewing geometry are fixed, the sea surface behaves as a continuously evolving system of liquid

facets. These facets, due to their transient orientation, refract incoming radiation at varying angles. Once refracted into the water column, the radiation travels downward, interacts with the seabed, and then ascends toward the surface.

Assuming a static seabed, such as sandy substrates, which remain relatively stable over short time scales, the upward radiation undergoes diffuse attenuation. In contrast, vegetated substrates (e.g., *Posidonia oceanica* meadows) oscillate due to hydrodynamic eddies, introducing additional variability in the radiative signal.

Upon reaching the sea surface from below, the emergent radiation is again refracted through the dynamic interface of liquid facets. The orientation of these facets determines the exit direction of the refracted signal, which varies temporally and spatially. Simultaneously, a portion of the incident radiation is reflected at the air-water interface. This specular reflection is also facet-dependent and contributes to the total radiance received by the satellite sensor.

Thus, the radiance vector reaching the sensor comprises both refracted emergent components and reflected incident components, each modulated by the instantaneous geometry of the surface facets. Despite selecting only six high-quality PlanetScope images from a potential daily dataset, chosen to minimize specular reflection, residual artifacts persist in scattered pixels.

Rather than pursuing a purely theoretical treatment of these phenomena [47], we propose a practical, image-based approach that leverages the high spatial resolution of PSB.SD imagery.

For given depth, optical water column characteristics and bottom reflectance, the reflectance variations (and indeed minima and maxima) are associated with the instantaneous orientation of water facets at the time of acquisition. These orientations, indeed, influence the emergent radiance through three main mechanisms: (i) refraction at the air–water interface of the incident radiation, (ii) refraction at the water–air interface of the emergent radiation, and (iii) reflection of the incident radiation by the liquid facets at the surface. These three main mechanisms modulate both emergent and reflected radiations. We aim to obtain emergent radiance from liquid facets oriented in a uniform position, also avoiding specular reflection phenomena, that is, facet orientations that generate maxima in reflectance, and also avoiding orientations that produce minima in reflectance. It needs to be highlighted that it is not necessary to determine the optimal orientation of the liquid facets, since the algorithm is calibrated against in situ reference data.

Considering that these maxima and minima depend not only on the geometric configuration—incident solar radiation direction, instantaneous facet orientation, and sensor viewing geometry—but also on the relative size of the liquid facets with respect to the geometric resolution of the imagery (which, moreover, is obtained through resampling). To identify and mitigate these, we applied a focal operator that evaluates the recurrence of local maxima and minima within a 3×3 moving window and thereby inferring the average orientation and exposure of liquid facets at the image resolution scale.

Two filtering strategies were tested, named FREO, an acronym for Focal Reflectance Extremes Operator:

- FREO1: only pixels that are always local maxima or minima (mask value = 9) are replaced.
- FREO2: all pixels that are ever local maxima or minima (mask value ≥ 1) are replaced.

In the FREO1 method, which represents the more conservative strategy, we replace only those pixels that consistently behave as local maxima or local minima across all observations (focal samples). In other words, intervention is limited to pixels marked with a mask value of 9, meaning they always exhibit an extreme value. In contrast, the FREO2 method adopts a less conservative approach: it replaces all pixels that behave as local

maxima or minima at least once. Here, the criterion is broader, since all pixels with a mask value equal to or greater than 1 are included. This procedure was applied independently to each spectral band to account for the PlanetScope image generation process. Specifically, the PSB.SD telescope acquires bands sequentially using a push-frame mechanism. Frames are stacked to form band-specific images, and scenes are generated via a homographic transformation across multiple frames. Since this process is performed independently for each band, reflective pixel positions may differ across bands.

Therefore, the filtering and replacement of extreme reflectance pixels were conducted per band. Missing values were filled using a recursive mean filter (3×3 window) until all no-data pixels were interpolated. This approach is expected to narrow the error band in bathymetric estimation. In particular, it is expected that the more aggressive FREO2 strategy will yield a tighter confidence interval. It is essential to note that bathymetry is inferred from the attenuation of radiation along an optical path that is inclined rather than vertical. However, the estimated depth is assigned to the vertical projection.

2.11. Depth-Dependent K_d

An assumption in SDB is that the diffuse attenuation coefficient remains spatially constant throughout the study area. This leads to a linear alignment of pixels in the logarithmic domain of reflectance values. However, when K_d varies spatially, this assumption no longer holds, and nonlinear deviations may emerge in the reflectance-depth relationship. Several natural processes can contribute to such variability in water column attenuation, including sediment resuspension due to hydrodynamic forcing, among others. In this case, it is therefore reasonable to hypothesize that K_d may vary with depth itself.

Under this condition, the radiative transfer equation transforms into a second-order polynomial. While this approach can effectively compensate for nonlinear deviations and improve depth estimation accuracy, polynomial models are generally less suitable for extrapolation beyond the calibration domain, which represents a clear limitation of the method.

The hypothesis of a linearly variable K_d with depth was tested according to the following relationship (4):

$$K_d = m_{K_d} Z + q_{K_d} \tag{4}$$

where m_{K_d} rules the K_d variation with water depth, while q_{K_d} quantify its spatially constant component. Under this assumption, Equation (1) can be expressed as a second-order polynomial function (5):

$$ln(\langle \rho_0 \rangle - \rho_\infty) = ln(\rho_b - \rho_\infty) - 2m_{K_d} Z^2 - 2q_{K_d} Z \tag{5}$$

where $\langle \rho_0 \rangle$ denotes the reflectance layer, Z corresponds to the multibeam reference data, and all remaining parameters are calibrated against these reference data.

The performance of the algorithm is assessed on the calibration dataset using the coefficient of determination, R^2 (–), and the root mean square error, *RMSE* (m), computed between MB and SDB depths (Z_{mb} and Z_{op}, respectively). For the validation dataset, the summary table includes a more comprehensive set of statistics: the Slope (–), mean bias error, *MBE* (m), mean absolute error, *MAE* (m), concordance correlation coefficient, *CCC* (–), median absolute distance, *MAD* (m), and *Error* (%). All statistical formulas are reported below (respectively, (6a–h)).

$$R^2 = 1 - \frac{\sum_{i=1}^{n} \left(z_{op,i} - \widehat{z_{op,i}} \right)^2}{\sum_{i=1}^{n} \left(z_{op,i} - \mu_{op} \right)^2} \tag{6a}$$

$$RMSE = \sqrt{\frac{1}{n}\sum_{i=1}^{n}\left(z_{op,i} - z_{mb,i}\right)^2} \tag{6b}$$

$$MBE = \frac{1}{n}\sum_{i=1}^{n}\left(z_{op,i} - z_{mb,i}\right) \tag{6c}$$

$$MAE = \frac{1}{n}\sum_{i=1}^{n}\left|z_{op,i} - z_{mb,i}\right| \tag{6d}$$

$$MAD = median\left(\left|z_{op,i} - z_{mb,i} - median\left(z_{op,i} - z_{mb,i}\right)\right|\right) \tag{6e}$$

$$Slope = \frac{\sum_{i=1}^{n}\left(z_{mb,i} - \overline{z_{mb}}\right)\left(z_{op,i} - \overline{z_{op}}\right)}{\sum_{i=1}^{n}\left(z_{mb,i} - \overline{z_{mb}}\right)^2} \tag{6f}$$

$$CCC = \frac{2\sigma_{mb,op}}{\sigma_{mb}^2 + \sigma_{op}^2 + \left(\mu_{mb} - \mu_{op}\right)^2} \tag{6g}$$

$$Error = \frac{RMSE}{\mu_{mb}} \tag{6h}$$

where

- $\widehat{z_{op,i}}$: The regression model estimate;
- $\sigma_{mb,op}$: The covariance between z_{mb} and z_{op};
- σ_{mb}^2, σ_{mb}^2: The variances;
- μ_{mb}, μ_{op}: The average values.

3. Results

From 1 January 2022, to 31 December 2023, despite the nominal daily revisit interval, applying a cloud cover filter set to 0% of the total area resulted in a total of 59 images. In this set, considering only images with low water turbidity, 21 images were identified. Ultimately, excluding images with elevated surface radiometric disturbance, suspended material in the water column, sun glint or other artifacts, resulted in a final set of 6 images, 2 from 2022 and 4 from 2023 (see Table 3).

Table 3. Preliminary data screening encompassed three steps: exclusion of cloudy images, selection of images that visually exhibited low water turbidity, exclusion of images with high surface perturbations such as sea waves or wind effects.

Criteria	Filtered Images
Clear Sky (cloud cover 0%)	59
-Clear Water	21
-No/Low Surface Radiometric Disturbances	6

Figure 4 illustrates representative cases of images excluded from the final dataset due to various quality issues. These include atmospheric haze, surface disturbances caused by wind and marine currents, capillary waves, suspended dissolved materials, and cloud shadows. Incorporating these scenes would add noise to the up-coming signal, resulting in biased depth estimates, especially in shallow waters characterized by high optical complexity.

The applicability of the methodology presented in this study is limited to the maximum depth where reflectance reaches an almost constant value regardless of depth, representing the value of an infinitely deep water column (see Equation (1)). The findings of spectral bands penetrability assessment are presented in Figure 5, indicating that the most effective bands for depth retrieval, among those provided by the PSB.SD sensors, are the second,

third, and fourth bands, corresponding, respectively, to wavelengths of 490, 531, and 565 nm. These bands make it possible to retrieve depth information up to ~25 m.

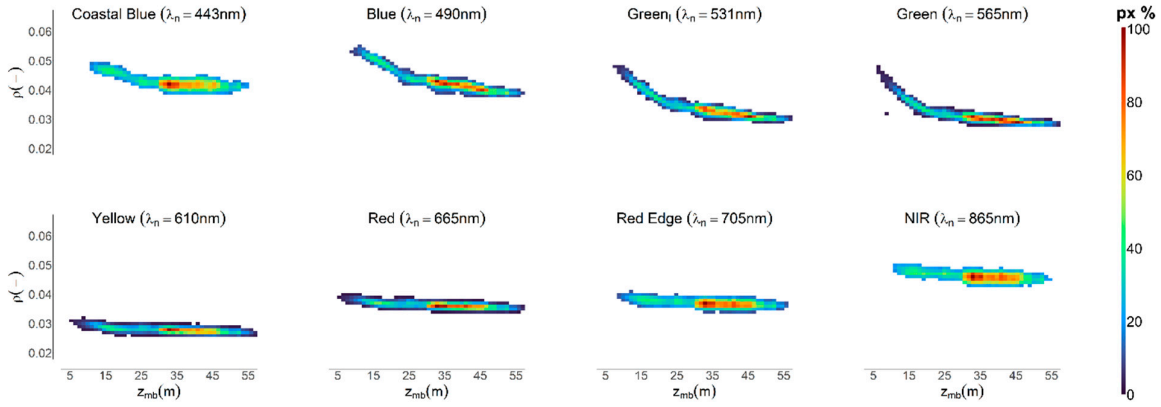


Figure 5. Reflectance (14 July 2022) for different bands vs. MB. Blue-Green wavelengths penetrate more into the water body, as shown in the upper plots, particularly the centre-left (B2: 490 nm), centre-right (B3: 531 nm), and right (B4: 565 nm). A decaying exponential relationship is clear for these spectral bands, as reflectance rapidly decreasing with increasing bathymetry. Pixel density is displayed using the 'turbo' colormap, which indicates the percentage relative to a total sample of 1×10^5 pixels. The same scale is used hereafter for all other density plots presented in this study.

Reflectances ρ_{490}, ρ_{531}, and ρ_{565} were visually identified as the most relevant for bathymetric retrieval, since they vary significantly with bathymetry, following an exponential decay (see Equation (1)). Thus, they were employed to study the bathymetry derivability from each of the six selected time points, according to Section 2.1. Table 4 reports acquisition time, sun azimuth, sun elevation, satellite azimuth, view angle, and Ground Sampling Distance (GSD) of the six selected acquisition dates.

Table 4. Relevant metadata from images selected through the *Preliminary data screening*. The image from 30 July 2023, is a composite of two consecutive acquisition times.

Date (dd/mm/yyyy)	Time (ISO 8601 [48])	Sun Azimuth (°)	Sun Elevation (°)	Satellite Azimuth (°)	View Angle (°)	GSD (m)
14/07/2022	08:56:49.984932Z	108.8	57.0	100.9	5	4.0
16/07/2022	09:47:46.965535Z	124.3	65.1	277.6	5	3.9
27/06/2023	08:59:19.657603Z	107.4	58.5	268.2	1	3.7
30/07/2023	09:41:02.374703Z	125.8	61.8	277.9	5	3.7
	09:41:45.846475Z	126.4	62.2	277.7	5	3.7
15/08/2023	09:01:27.448719Z	119.8	52.6	275.6	2.6	3.6
28/09/2023	09:03:25.504429Z	139.4	42.5	148.4	0.1	3.9

MB and SDB have been compared for the selected acquisition times, considering just the three optimal spectral bands (Table 5). The R^2 values obtained indicate that not all the images are suitable for estimating bathymetry. In particular, the most suitable images are the two acquired in July 2022 and the one in June 2023. Furthermore, in almost all cases, ρ_{531} spectral reflectance proves to be the most effective, reporting the highest R^2 values.

Table 5. R^2 resulting from the correlation of MB and SDB obtained using single spectral bands for single time points. Best accuracy for Green_I (531 nm) and for the 14 July 2022. In grey are highlighted very strong correlations [49] ($R^2 > 0.64$). In bold, the date-band combination that exhibits the highest correlation value.

R^2	2022			2023		
λ (nm)	14/07	16/07	27/06	30/07	15/08	28/09
490	0.839	0.667	0.685	0.437	0.152	0.005
531	**0.915**	0.856	0.714	0.594	0.694	0.411
565	0.908	0.847	0.678	0.515	0.746	0.544

After the evaluation of the single data layers' output, the effectiveness of applying spectral averaging or temporal averaging to improve bathymetric estimation was evaluated. Preliminary results (Figure 5, Table 5) guided the selection of a refined dataset, restricting it to the three most penetrating bands (ρ_{490}, ρ_{531}, ρ_{565}) and the three most consistent images (14 July 2022, 16 July 2022, 27 June 2023).

Spectral averaging effectiveness was tested by comparing results obtained using a single band with the average of two bands or the average of three bands. The corresponding R^2 values are reported in Table 6.

Table 6. Spectral average. R^2 resulting from MB and SDB obtained using single time points for different band combinations. Best accuracy (in bold) when averaging Band 3 (531 nm) and Band 4 (565 nm) for the 14 July 2022. Values surrounded by a dashed box denote the two best spectral combinations.

R^2	2022		2023
λ (nm)	14/07	16/07	27/06
490 531	0.917	0.834	0.719
490 565	0.922	0.838	0.702
531 565	**0.933**	0.886	0.713
490 531 565	0.930	0.872	0.719

Temporal averaging was then evaluated to determine its potential advantages over single-image bathymetric estimation. The outcomes are reported in Table 7.

Table 7. Time average. R^2 from MB and SDB using single bands across time points combinations. Best accuracy (in bold) averaging images from 2022 using Band 3 (531 nm). Values surrounded by a dashed box denote the two most suitable acquisition time combinations.

R^2	14/07 16/07	14/07	16/07 27/06	14/07 16/07	2022
λ (nm)		27/06		27/06	2023
490	0.866	0.819	0.762	0.849	
531	**0.934**	0.853	0.811	0.888	
565	0.923	0.823	0.787	0.866	

Finally, the two approaches were combined to evaluate whether the integration of temporal and spectral averaging enhances bathymetric accuracy, making it more consistent with multibeam measurements. Table 8 presents the R^2 values for the optimal combinations—relative to the results previously obtained (see Tables 6 and 7). The results specifically highlight that in the case study, the most accurate bathymetric estimation is achieved by averaging spectral reflectances ρ_{531} and ρ_{565} acquired on both 14 and 16 July 2022, achieving a peak R^2 value of 0.946. The addition of the 490 nm blue band does not systematically improve bathymetric performance and may, in some cases, slightly degrade accuracy. This behavior is likely driven by the increased susceptibility of shorter wavelengths to scattering processes and photosynthetic absorption within the water column in

coastal waters. Therefore, the ρ_{490} reflectance reduces the overall signal to noise ratio of this spectral combination. Similarly, adding the acquisition from 27 June 2023, to the temporal combination does not result in improved accuracy and produces a slight degradation. This indicates that temporal averaging is most effective when applied to scenes acquired under comparable optical conditions.

Table 8. R^2 resulting from MB and SDB obtained using spectral average for time average. In bold, the combination that exhibits the highest correlation value.

R^2 λ (nm)	2022 14/07 16/07	2022 2023 14/07 16/07 27/06
531 565	**0.946**	0.887
490 531 565	0.943	0.888

These findings are consistent with Casal et al. (2019), who showed that in optically complex coastal waters the green spectral band around 550 nm conveys stronger and more stable depth-related information than the blue band [50].

Based on the preliminary results obtained, the dataset was further reduced for more detailed analyses by retaining only the spectral bands 3 and 4 from 2022 images. The accuracy achieved with the best-performing single data layer (band 3, 14 July) was then evaluated in comparison to spectral and/or temporal combinations.

The relation between MB (Z_{mb}) and reflectance reported in Figure 6, is best described using an exponential decay of the type $\rho = a{\cdot}e^{-bZ} + c$, where with respect to Equation (1): a represents $\rho_b - \rho_\infty$, b corresponds to $2K_d$ and c is analogous to $\rho_0 - \rho_\infty$.

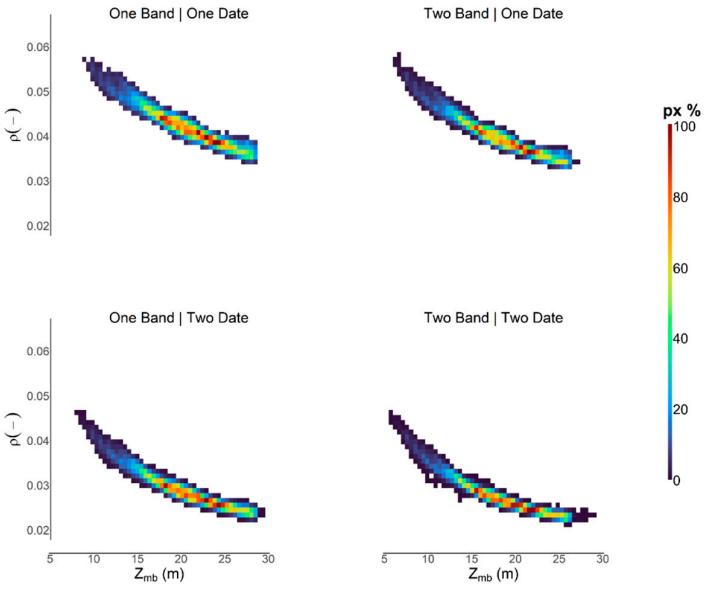


Figure 6. Model assessment using the Band 3 (531 nm) or the average of Band 3 and Band 4 (531 nm, 565 nm) relying on a single image (14 July 2022) or the average of two images (14 and 16 July 2022), exclusively in sandy bottom over 1×10^3 random points.

From Equation (3), $\langle \rho_0 \rangle$ (reflectance) and Z (multibeam depths) are known, whereas all remaining parameters are calibrated based on these reference data.

The model exhibited the best performance when calibrated using the two-green spectral average (ρ_{531} and ρ_{565}) derived from the mean reflectance of 2022 images (Table 8, Figure 7). This approach significantly reduced error metrics, highlighting the advantages of integrating data across different spectral bands and time points to enhance the robustness and accuracy of depth estimation (Table 9).

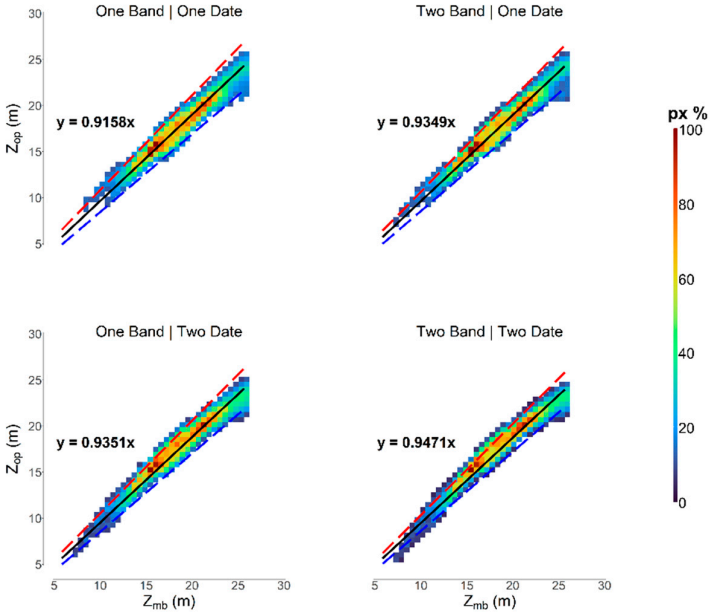


Figure 7. Validation of SDB (Z_{op}) compared to MB (Z_{mb}), exclusively in sandy bottom over 1×10^3 random points (different respect to calibration set). The blue and red dashed lines, corresponding to the lower (P5) and upper (P95) linear trends, respectively, delineate the 95% confidence interval, where half the interval width indicates the error.

Table 9. RMSE (m) for all the best combinations.

RMSE λ (nm)	14 July 2022	14–16 July 2022
531	1.09	0.96
531 565	0.96	0.84

Validation scatterplots show a gradual increase in accuracy as more input layers are incorporated. In Figure 7, the single data layer "One-Band | One-Date" (referring to ρ_{531} reflectance from 14 July 2022) exhibits the highest dispersion, with an error of ±10.1% respect to MB. From "Two-Band | One-Date" and "One-Band | Two-Date" dispersion decreases, with errors of ±8.6% and ±8.7%, respectively. The combination of spectral and temporal averaging results in the lowest observed error, equals to ±7.3% (Table 10).

Table 10. Trendline slope and dispersion for tested configurations.

	Trendline Slope	Dispersion (%)
One-Band | One-Date	0.916	±10.1
Two-Band | One-Date	0.935	±8.6
One-Band | Two-Date	0.935	±8.7
Two-Band | Two-Date	0.947	±7.3

These findings indicate a strong correlation between SDB and multibeam data, which allowed us to accurately estimate bathymetry down to approximately 25 m. The intercept was constrained to zero to ensure that the trend line passes through the origin of the Cartesian axis. As a result, the estimated bathymetry on the shoreline is null. Table 11 indicates that the "Two-Band | Two-Date" configuration allows obtaining the most accurate result.

Table 11. Summary table reporting different error metrics for all best combinations tested over the 1×10^5 points used for validation. By columns: R square, slope of linear regression, mean bias error, root mean square error, mean absolute error, concordance correlation coefficient, median absolute deviation, and error calculated as half the width of the confidence interval (95%); by row: basic layer without noise reduction, conservative noise reduction (FREO1), non-conservative noise reduction (FREO2), and non-conservative noise reduction considering a depth-dependent K_d. Layer combination key: A = One-Band | One-Date; B = Two-Band | One-Date; C = One-Band | Two-Date; D = Two-Band | Two-Date. The capital lambda symbol (∧) denotes a processing step (1–4) in combination with FREO and/or depth-dependent K_d corrections.

Processing Step	Input Layer	R^2 (m)	Slope (-)	MBE (m)	RMSE (m)	MAE (m)	CCC (-)	MAD (-)	Error (%)
1: no average	A	0.915	0.916	0.005	1.088	0.851	0.956	1.044	10.127
2: spectral average	B	0.933	0.935	0.003	0.962	0.751	0.966	0.926	8.692
3: time average	C	0.934	0.935	0.001	0.956	0.758	0.966	0.954	8.746
4: time and spectral average	D	0.946	0.947	0.001	0.863	0.68	0.972	0.848	7.282
1 ∧ FREO1	A	0.923	0.924	0.005	1.034	0.811	0.96	1.002	9.64
2 ∧ FREO1	B	0.938	0.94	0.003	0.926	0.724	0.968	0.895	8.327
3 ∧ FREO1	C	0.941	0.942	0.001	0.908	0.722	0.969	0.911	8.262
4 ∧ FREO1	D	0.95	0.951	0.001	0.83	0.654	0.975	0.815	7.022
1 ∧ FREO2	A	0.941	0.942	0.004	0.909	0.713	0.969	0.882	8.499
2 ∧ FREO2	B	0.948	0.949	0.002	0.849	0.663	0.973	0.816	7.641
3 ∧ FREO2	C	0.953	0.954	0.001	0.807	0.645	0.976	0.821	7.477
4 ∧ FREO2	D	0.958	0.959	0.001	0.761	0.601	0.979	0.745	6.426
1 ∧ FREO2 ∧ K_d (Z)	A	0.942	0.943	0.004	0.896	0.703	0.97	0.864	8.721
2 ∧ FREO2 ∧ K_d (Z)	B	0.949	0.95	0.002	0.844	0.658	0.974	0.806	7.744
3 ∧ FREO2 ∧ K_d (Z)	C	0.957	0.959	0.001	0.769	0.618	0.978	0.793	7.057
4 ∧ FREO2 ∧ K_d (Z)	D	0.966	0.967	0.001	0.688	0.55	0.983	0.712	5.973

As described at the end of Section 2, we applied a noise-reduction technique starting from the reflectance layers. The following scatterplots (Figures 8 and 9) illustrate the validation results after this correction, where a clear narrowing of the error can be observed, indicating an overall improvement in accuracy.

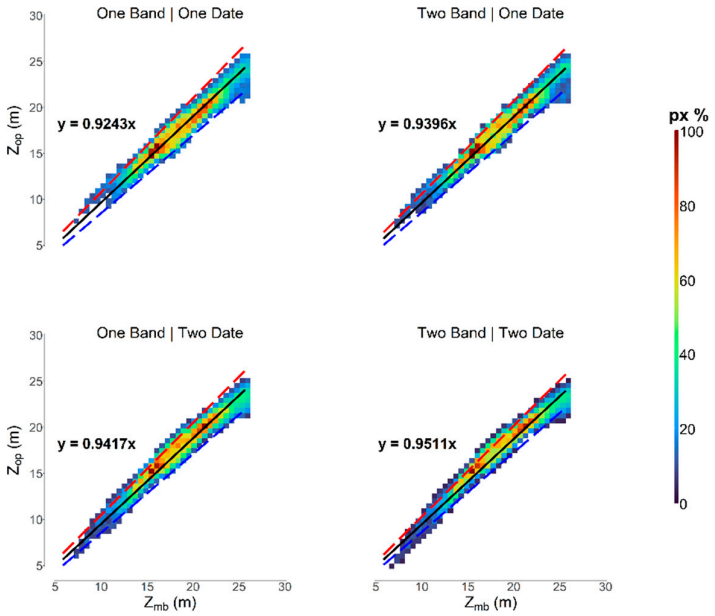


Figure 8. Validation of SDB (Z_{op}) compared to MB (Z_{mb}) for the conservative, FREO1, corrected data.

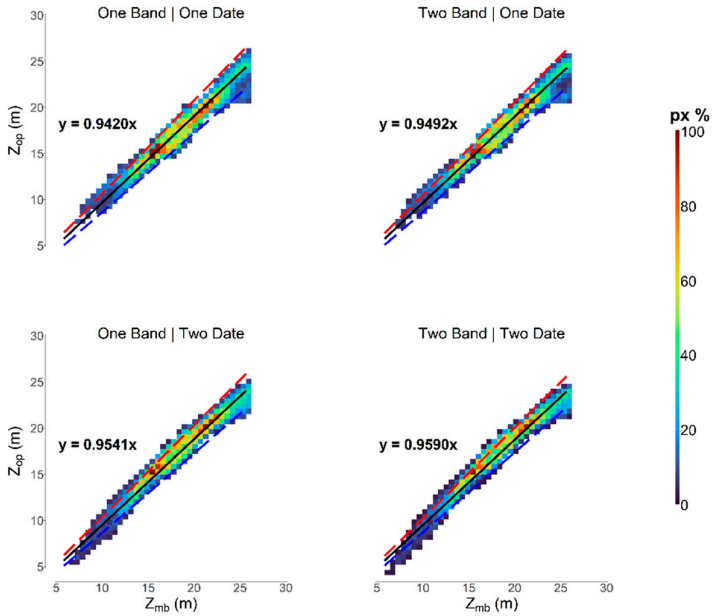


Figure 9. Validation of SDB (Z_{op}) compared to MB (Z_{mb}) for the non-conservative, FREO2, corrected data.

Noise reduction using the conservative approach (FREO1) slightly improved the overall accuracy across all four best combinations, yielding an optimal error of ±7.0%. Conversely, removing a larger portion of noise using the non-conservative mode (FREO2) resulted in a greater improvement, with an optimal error value of ±6.4%.

Regarding the "One-Band | One-Date" configuration, the data from the 16th of July 2022 is characterized by a nonlinear behavior: the SDB does not change linearly with MB. This can be explained by the recognized principle that K_d is not uniform throughout the study domain, but rather shows a depth-dependent variability [51,52]. The scatterplots in Figure 10 show a linear pattern for the data from 14 July, with low dispersion, whereas the data from 16 July, despite also having low dispersion, exhibits nonlinearity. A logarithmic fit appears to better represent the observed distribution.

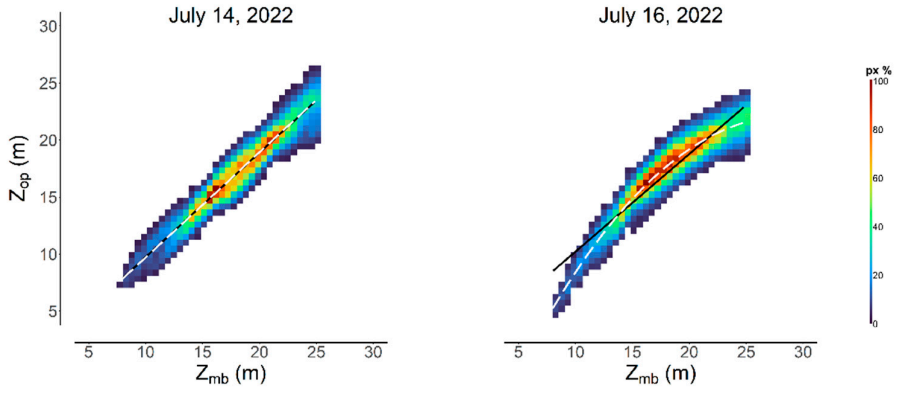


Figure 10. Density plots showing the correlation between MB (Z_{mb}) and SDB (Z_{op}) obtained from the band 3 on 14 and 16 July 2022. The black line represents the linear regression fit, while the white dashed line denotes the LOESS smoothing curve, highlighting the local trend. The distribution for 16 July exhibits nonlinearity. A logarithmic fit appears to better represent this distribution, meaning that the K_d varies with depth.

The nonlinear behavior observed on 16 July is also evident in the combined dates layer (Figure 11). Consequently, while time-averaging mitigates dispersion, it introduces a nonlinear pattern, which becomes particularly pronounced beyond a certain depth.

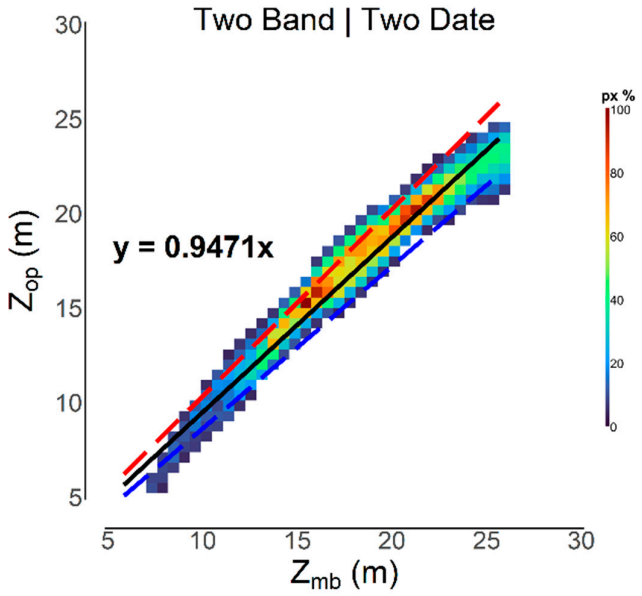


Figure 11. Although a linear trend appears to provide an acceptable fit, a logistic trend could better describe the distribution obtained by combining different dates. This non-linearity is introduced by reflectance from 16 July.

Considering this nonlinearity, caused by a depth-dependent variability of K_d, which is particularly evident in the image acquired on 16 July, Equation (5) was applied. The resulting fit proved to be even more satisfactory, as illustrated in the scatterplot in Figure 12, which finally displays a clear linearity even at shallow depth in the relationship between the SDB and MB, with an error value of ±5.9%.

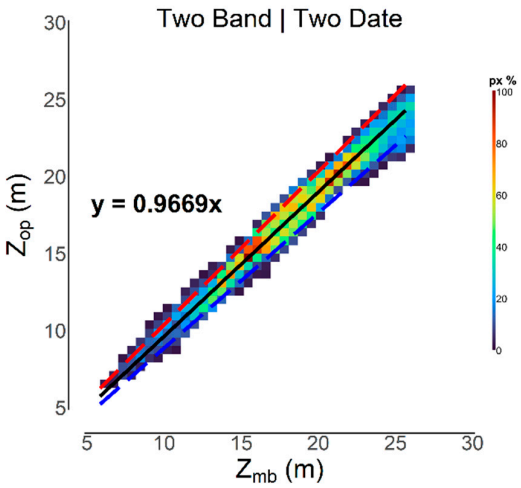


Figure 12. Best result density plot. Considering a depth-dependent K_d results in a linear trend with low dispersion also for shallow depths.

A consistent improvement can be observed across all the analyzed combinations, confirming the effectiveness of the proposed noise-reduction strategy and variable K_d hypothesis, as summarized by Table 11.

Figure 13 provides a visual representation of the progressive decrease in percentage error across the steps of the proposed methodological framework.

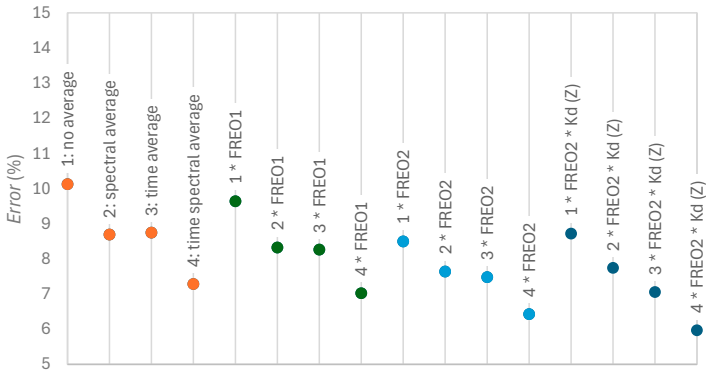


Figure 13. Percentage error of satellite-derived bathymetry relative to multibeam bathymetry, showing a progressive reduction across tested combinations.

The final outcomes are presented in Figure 14, which depicts a bathymetric map combining the SDB, accurate down to approximately 25 m, with the MB extending to depths of about 50 m. Where depth data is missing, a possibility could be to consider performing a geospatial interpolation to achieve full spatial coverage of the study area; however, this extension lies beyond the scope of the present work.

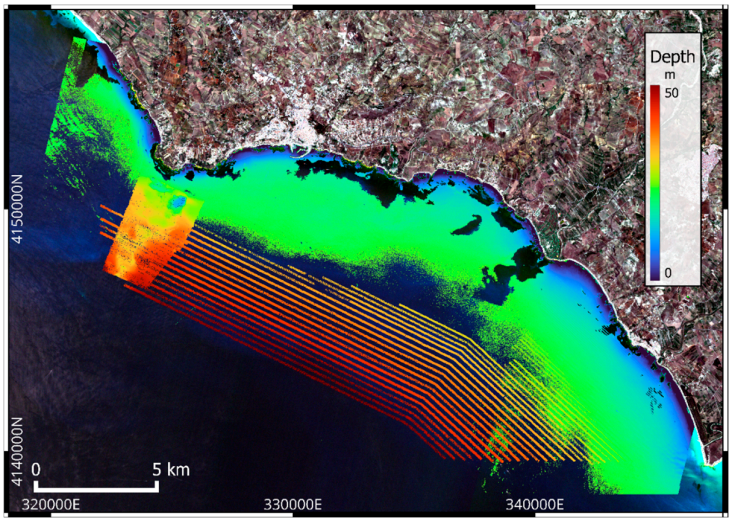


Figure 14. Pseudo color representation of the MB and SDB obtained using the best combination identified in this study (ρ_{531} and ρ_{565} acquired on both 14 and 16 July 2022, noise-reduction FREO2, depth-dependent K_d). Vegetated areas, boats and artifacts have been excluded. The multibeam layer is displayed on top of the optically derived layer; by applying an identical color scale to both datasets, a strong correspondence can be visually identified in the range of 5 to 25 m depth.

4. Discussion

Our work described a novel approach to improve Satellite-Derived Bathymetry accuracy in nearshore areas. The combination of various spectral bands and acquisition times allowed us to accurately estimate the water depth in the white ribbon zone down to approximately 25 m, producing an accurate bathymetric map. Validating with respect to multibeam measurements, we obtained a dispersion of approximately $\pm 6\%$ with a 95% confidence interval.

In general, averaging reflectance values across multiple bands or time points produced more robust and consistent data, reducing errors associated with single-layer perturbations and mitigating surface artifacts. However, this averaging improved data quality only in specific cases, as detailed in Section 3.

When the link between reflectance and multibeam measurements is not well described by a logarithmic relationship, the resulting bathymetric estimation error impacts the temporal averaging process embedded within the optimal configuration identified in this study: "Two-Band | Two-Date". To overcome this bias, we re-estimated the bathymetry by accounting for a depth-dependent K_d (Equation (4)), resulting in an SDB that varies linearly with the validation measurements.

The presented methodological approach reveals some limitations: initial image selection is based on visual screening; surface effects can significantly influence the results; radiometric contributions from surface phenomena, such as sun glint and wave patterns, further complicate the analysis; heterogeneity in the water column introduces further bias.

Besides these, the temporal mismatch of satellite imagery could represent a significant driver of variability, given that all datasets are calibrated against a multibeam dataset acquired between February and May 2023, while the satellite images themselves have been acquired in the summer seasons of 2022 and 2023. This temporal discrepancy poses challenges in shallow water/nearshore areas that exhibit rapid seabed morphological changes—such as Sciacca offshore. Future work will aim to mitigate these effects through (i) multi-epoch image compositing to reduce scene-specific noise and transient surface conditions, (ii) tidal normalization and water-level corrections where ancillary information is available, and (iii) improved spatial co-registration between datasets to minimize apparent depth differences caused by geometric misalignment.

While the spectral averaging forces the theoretical framework of the radiative transfer equation, which posits that the K_d is inherently dependent on wavelength, it clearly reduces the spread around the regression line.

5. Conclusions

In general, aggregating reflectance values over several spectral bands and acquisition times minimized errors associated with a single data layer by mitigating surface radiometric perturbations of the dynamic sea water facets. However, the averaging process only enhanced data quality under specific circumstances, most notably when applied to the July 2022 dataset, which already exhibited sharper and more coherent spectral features.

The satellite optical approach presents the drawback that the reflectance variability, depending on the emerging radiance signal, reaches a penetrability limit, depending on the characteristics of the water column, around 25–30 m in the case study water. However, this approach supports cost-effective, high-resolution mapping of water depth across extensive coastal zones, achieving metric-level accuracy and offering a favorable cost–benefit balance.

This study primarily shows that an integrated use of spectral, temporal, and depth-related information can significantly strengthen the robustness of SDB, as opposed to approaches based on individual scene optimization or elaborate data-fusion methodologies. The proposed combination of spectral-averaging with time-averaging enabled the generation of much cleaner informational layers, substantially reducing error metrics.

Future developments of the liquid-facets-dependent noise-reduction approach may also include frequency-domain analyses, in which the data are transformed from the spatial to the frequency domain, filtered, and then converted back to the spatial domain. Such frequency-domain investigations could offer deeper insight into the spectral components that characterize the radiometric patterns induced by surface effects.

Future research should also investigate the influence of geometric-correction accuracy, potential inter-band spatial shifts, and spatial misalignment between optical satellite imagery and multibeam or other calibration data to provide deeper insight into the advantages and limitations of the current approach and to guide future improvements in data preprocessing.

Satellite altimeter-based calibration/validation deserves further study to broaden the applicability of the proposed methodology. Indeed, future research could benefit from comparative experiments involving alternative satellite platforms, which offer high-quality blue and green spectral bands and high revisit frequency. Moreover, integrating LIDAR satellite-based bathymetric data could provide an alternative layer of validation and calibration, especially in areas where acoustic measurements are unavailable or impractical. At first, altimeter-derived elevations may be employed as an independent validation dataset to evaluate SDB accuracy and spatial consistency beyond the extent of multibeam coverage. Secondly, selected altimetric measurements can serve as external depth constraints to stabilize the calibration process in regions characterized by sparse in situ data or pronounced optical variability. More advanced integration approaches constitute promising avenues for future research but are beyond the scope of the present study. These comparative analyses would help assess the scalability and adaptability of the proposed spectral–temporal averaging framework across different sensor architectures and observational strategies.

Author Contributions: Conceptualization, Methodology, Software, Validation, Formal analysis, Data curation, Visualization, Investigation—A.M., V.L.P. and G.A.N.; Resources, Project administration, Funding acquisition—A.S.; Writing—original draft—G.A.N. and A.M.; Writing, review, and editing—A.M., V.L.P., G.A.N. and A.S.; Supervision—A.S. and A.M. All authors have read and agreed to the published version of the manuscript.

Funding: This research is supported under the National Recovery and Resilience Plan (NRRP), Mission 4 Component 2 Investment 1.4—Call for tender No. 3138 of 16 December 2021, rectified by Decree n.3175 of 18 December 2021 of Italian Ministry of University and Research funded by the European Union—under the NextGenerationEU initiative. Project code CN_00000033, Concession Decree No. 1034 of 17 June 2022 adopted by the Italian Ministry of University and Research, CUP: B73C22000790001, Project title "National Biodiversity Future Center—NBFC".

Data Availability Statement: The analytical procedures were carried out using the R studio (language version 4.5.1) and QGIS software (version 3.40.8), adhering to an open-source environment. The full script is available upon request to the authors.

Acknowledgments: PSB.SD images were made available by Planet Labs Inc. (San Francisco, CA, USA) within the Planet's Education and Research (E and R) Program.

Conflicts of Interest: The authors declare no conflicts of interest.

Abbreviations

The following abbreviations are used in this manuscript:

SDB	Satellite-Derived Bathymetry
PSB.SD	PlanetScope SuperDove equipped with a PSBlue telescope
MB	Multibeam Bathymetry
FREO	Focal Reflectance Extremes Operator

References

1. Mayer, L.; Jakobsson, M.; Allen, G.; Dorschel, B.; Falconer, R.; Ferrini, V.; Lamarche, G.; Snaith, H.; Weatherall, P. The Nippon Foundation—GEBCO Seabed 2030 Project: The Quest to See the World's Oceans Completely Mapped by 2030. *Geosciences* **2018**, *8*, 63. [CrossRef]
2. The Nippon Foundation. GEBCO Seabed 2030 Announces Latest Progress on World Hydrography Day—Seabed 2030. Available online: https://seabed2030.org/2024/06/21/seabed-2030-announces-latest-progress-on-world-hydrography-day/ (accessed on 25 March 2025).
3. GEBCO Bathymetric Compilation Group. The GEBCO_2025 Grid—A Continuous Terrain Model of the Global Oceans and Land. 2025. Available online: https://www.gebco.net/data-products-gridded-bathymetry-data/gebco2025-grid/ (accessed on 20 November 2025).

4. Ferreira, I.O.; Andrade, L.C.D.; Teixeira, V.G.; Santos, F.C.M. State of Art of Bathymetric Surveys. *Bol. Ciênc. Geod.* **2022**, *28*, e2022002. [CrossRef]
5. Gao, J. Bathymetric Mapping by Means of Remote Sensing: Methods, Accuracy and Limitations. *Prog. Phys. Geogr.* **2009**, *33*, 103–116. [CrossRef]
6. Li, Z.; Peng, Z.; Zhang, Z.; Chu, Y.; Xu, C.; Yao, S.; García-Fernández, Á.F.; Zhu, X.; Yue, Y.; Levers, A.; et al. Exploring Modern Bathymetry: A Comprehensive Review of Data Acquisition Devices, Model Accuracy, and Interpolation Techniques for Enhanced Underwater Mapping. *Front. Mar. Sci.* **2023**, *10*, 1178845. [CrossRef]
7. Leon, J.X.; Phinn, S.R.; Hamylton, S.; Saunders, M.I. Filling the 'White Ribbon'—A Multisource Seamless Digital Elevation Model for Lizard Island, Northern Great Barrier Reef. *Int. J. Remote Sens.* **2013**, *34*, 6337–6354. [CrossRef]
8. Weymer, B.A.; Everett, M.E.; Haroon, A.; Jegen-Kulcsar, M.; Micallef, A.; Berndt, C.; Michael, H.A.; Evans, R.L.; Post, V. The Coastal Transition Zone Is an Underexplored Frontier in Hydrology and Geoscience. *Commun. Earth Environ.* **2022**, *3*, 323. [CrossRef]
9. Carvalho, R.C.; Hamylton, S.; Woodroffe, C.D. Filling the 'White Ribbon' in Temperate Australia: A Multi-Approach Method to Map the Terrestrial-Marine Interface. In Proceedings of the 2017 IEEE/OES Acoustics in Underwater Geosciences Symposium (RIO Acoustics), Rio de Janeiro, Brazil, 25–27 July 2017; pp. 1–5.
10. Kotilainen, A.T.; Kaskela, A.M. Comparison of Airborne LiDAR and Shipboard Acoustic Data in Complex Shallow Water Environments: Filling in the White Ribbon Zone. *Mar. Geol.* **2017**, *385*, 250–259. [CrossRef]
11. Asiyabi, R.M.; Ghorbanian, A.; Tameh, S.N.; Amani, M.; Jin, S.; Mohammadzadeh, A. Synthetic Aperture Radar (SAR) for Ocean: A Review. *IEEE J. Sel. Top. Appl. Earth Obs. Remote Sens.* **2023**, *16*, 9106–9138. [CrossRef]
12. Pereira, P.; Baptista, P.; Cunha, T.; Silva, P.A.; Romão, S.; Lafon, V. Estimation of the Nearshore Bathymetry from High Temporal Resolution Sentinel-1A C-Band SAR Data—A Case Study. *Remote Sens. Environ.* **2019**, *223*, 166–178. [CrossRef]
13. Ashphaq, M.; Srivastava, P.K.; Mitra, D. Review of Near-Shore Satellite Derived Bathymetry: Classification and Account of Five Decades of Coastal Bathymetry Research. *J. Ocean. Eng. Sci.* **2021**, *6*, 340–359. [CrossRef]
14. Duplančić Leder, T.; Baučić, M.; Leder, N.; Gilić, F. Optical Satellite-Derived Bathymetry: An Overview and WoS and Scopus Bibliometric Analysis. *Remote Sens.* **2023**, *15*, 1294. [CrossRef]
15. Ma, Y.; Xu, N.; Liu, Z.; Yang, B.; Yang, F.; Wang, X.H.; Li, S. Satellite-Derived Bathymetry Using the ICESat-2 Lidar and Sentinel-2 Imagery Datasets. *Remote Sens. Environ.* **2020**, *250*, 112047. [CrossRef]
16. Szafarczyk, A.; Toś, C. The Use of Green Laser in LiDAR Bathymetry: State of the Art and Recent Advancements. *Sensors* **2023**, *23*, 292. [CrossRef] [PubMed]
17. Mohammadloo, T.H.; Snellen, M.; Simons, D.G. Multi-Beam Echo-Sounder Bathymetric Measurements: Implications of Using Frequency Modulated Pulses. *J. Acoust. Soc. Am.* **2018**, *144*, 842–860. [CrossRef] [PubMed]
18. Wilson, M.F.; O'Connell, B.; Brown, C.; Guinan, J.C.; Grehan, A.J. Multiscale Terrain Analysis of Multibeam Bathymetry Data for Habitat Mapping on the Continental Slope. *Mar. Geod.* **2007**, *30*, 3–35. [CrossRef]
19. Figueira, W.; Ferrari, R.; Weatherby, E.; Porter, A.; Hawes, S.; Byrne, M. Accuracy and Precision of Habitat Structural Complexity Metrics Derived from Underwater Photogrammetry. *Remote Sens.* **2015**, *7*, 16883–16900. [CrossRef]
20. Hatcher, G.A.; Warrick, J.A.; Ritchie, A.C.; Dailey, E.T.; Zawada, D.G.; Kranenburg, C.; Yates, K.K. Accurate Bathymetric Maps From Underwater Digital Imagery Without Ground Control. *Front. Mar. Sci.* **2020**, *7*, 525. [CrossRef]
21. Albright, A.; Glennie, C. Nearshore Bathymetry From Fusion of Sentinel-2 and ICESat-2 Observations. *IEEE Geosci. Remote Sens. Lett.* **2021**, *18*, 900–904. [CrossRef]
22. Forfinski-Sarkozi, N.A.; Parrish, C.E. Active-Passive Spaceborne Data Fusion for Mapping Nearshore Bathymetry. *Photogramm. Eng. Remote Sens.* **2019**, *85*, 281–295. [CrossRef]
23. Parrish, C.E.; Magruder, L.; Herzfeld, U.; Thomas, N.; Markel, J.; Jasinski, M.; Imahori, G.; Herrmann, J.; Trantow, T.; Borsa, A.; et al. ICESat-2 Bathymetry: Advances in Methods and Science. In Proceedings of the OCEANS 2022, Virginia Beach, VA, USA, 17–21 October 2022; pp. 1–6.
24. Zhang, X.; Ma, Y.; Li, Z.; Zhang, J. Satellite Derived Bathymetry Based on ICESat-2 Diffuse Attenuation Signal without Prior Information. *Int. J. Appl. Earth Obs. Geoinf.* **2022**, *113*, 102993. [CrossRef]
25. Sun, H.; Jin, T.; Liu, W.; Sun, H. Analysis of the Precision and Bias of ICESat-2 Sea Surface Height Product. *Mar. Geod.* **2025**, *48*, 239–257. [CrossRef]
26. NASA Web. Technical Specs | ICESat-2. Available online: https://icesat-2.gsfc.nasa.gov/science/specs (accessed on 6 May 2025).
27. Catalano, R.; Infuso, S.; Sulli, A. Tectonic History of the Submerged Maghrebian Chain from the Southern Tyrrhenian Sea to the Pelagian Foreland. *Terra Nova* **1995**, *7*, 179–188. [CrossRef]
28. Ghisetti, F.C.; Gorman, A.R.; Grasso, M.; Vezzani, L. Imprint of Foreland Structure on the Deformation of a Thrust Sheet: The Plio-Pleistocene Gela Nappe (Southern Sicily, Italy). *Tectonics* **2009**, *28*, TC4015. [CrossRef]

29. Maltese, A.; Presti, V.L.; Nocera, G.A.; Sulli, A. Comparison of Bathymetry Estimated from Multibeam Echosounder and Optical Data. In *Remote Sensing for Agriculture, Ecosystems, and Hydrology XXVI*; SPIE: Cergy-Pontoise, France, 2024; Volume 13191, pp. 26–32.
30. Srivastava, E.; Parrino, N.; Bonfardeci, A.; Agate, M.; Calederini, F.; Gasparo Morticelli, M.; Burrato, P.; Moscariello, A.; Dahali, M.; Malik, J.N.; et al. Unravelling Late Quaternary Coastal Evolution through a Multidisciplinary Approach: A Case Study from Southwestern Sicily (Italy). *AMQ* **2025**, *38*, 119–131. [CrossRef]
31. NASA Web. What Are SmallSats and CubeSats? Available online: https://www.nasa.gov/what-are-smallsats-and-cubesats/ (accessed on 26 March 2025).
32. Planet Labs PBC. PlanetScope Overview. Available online: https://developers.planet.com/docs/data/planetscope/ (accessed on 26 March 2025).
33. Planet Labs PBC. PlanetScope Instruments. Available online: https://developers.planet.com/docs/apis/data/sensors/ (accessed on 26 March 2025).
34. Aati, S.; Avouac, J.-P.; Rupnik, E.; Deseilligny, M.-P. Potential and Limitation of PlanetScope Images for 2-D and 3-D Earth Surface Monitoring With Example of Applications to Glaciers and Earthquakes. *IEEE Trans. Geosci. Remote Sens.* **2022**, *60*, 1–19. [CrossRef]
35. Planet Labs. Combined Imagery Product Spec FINAL | October 2025. Available online: https://assets.planet.com/docs/Planet_Combined_Imagery_Product_Specs_letter_screen.pdf (accessed on 23 December 2025).
36. Chavez, P.S. An Improved Dark-Object Subtraction Technique for Atmospheric Scattering Correction of Multispectral Data. *Remote Sens. Environ.* **1988**, *24*, 459–479. [CrossRef]
37. Gordon, H.R.; Morel, A.Y. Remote Assessment of Ocean Color for Interpretation of Satellite Visible Imagery: A Review. In *Lecture Notes on Coastal and Estuarine Studies*; American Geophysical Union: Washington, DC, USA, 1983; Volume 4, ISBN 978-0-387-90923-3.
38. Caldareri, F.; Sulli, A.; Parrino, N.; Dardanelli, G.; Todaro, S.; Maltese, A. On the Shoreline Monitoring via Earth Observation: An Isoradiometric Method. *Remote Sens. Environ.* **2024**, *311*, 114286. [CrossRef]
39. Caldareri, F.; Parrino, N.; Balsamo, L.; Dardanelli, G.; Todaro, S.; Sulli, A.; Maltese, A. Shoreline Time Series Analysis through the Isoradiometric Method: Bridging Landscape Evolution and Coastal Management. *Int. J. Appl. Earth Obs. Geoinf.* **2025**, *141*, 104618. [CrossRef]
40. Maltese, A.; Caldareri, F.; Parrino, N.; Todaro, S.; Dardanelli, G.; Sulli, A. A Radiometric Contouring Approach to Map the Shoreline. In *Remote Sensing for Agriculture, Ecosystems, and Hydrology XXV*; SPIE: Cergy-Pontoise, France, 2023; Volume 12727, pp. 57–66.
41. Lee, Z.; Carder, K.L.; Arnone, R.A. Deriving Inherent Optical Properties from Water Color: A Multiband Quasi-Analytical Algorithm for Optically Deep Waters. *Appl. Opt.* **2002**, *41*, 5755–5772. [CrossRef]
42. Morel, A.; Maritorena, S. Bio-Optical Properties of Oceanic Waters: A Reappraisal. *J. Geophys. Res. Ocean.* **2001**, *106*, 7163–7180. [CrossRef]
43. Wang, E.; Zhang, H.; Wang, J.; Cao, W.; Li, D. Simulation and Sensitivity Analysis of Remote Sensing Reflectance for Optically Shallow Water Bathymetry. *Remote Sens.* **2025**, *17*, 1384. [CrossRef]
44. Jain, S.C.; Miller, J.R. Algebraic Expression for the Diffuse Irradiance Reflectivity of Water from the Two-Flow Model. *Appl. Opt.* **1977**, *16*, 202–204. [CrossRef] [PubMed]
45. Moussa, H.B.; Viollier, M.; Belsher, E.T. Télédétection Des Algues Macrophytes de I'Archipel de Molene (France) Radiometrie de Terrain et Application Aux Donnees Du Satellite SPOT. *Int. J. Remote Sens.* **1989**, *10*, 53–69. [CrossRef]
46. Ciraolo, G.; Cox, E.; Loggia, G.L.; Maltese, A. The Classification of Submerged Vegetation Using Hyperspectral MIVIS Data. *Ann. Geophys.* **2006**, *49*. [CrossRef]
47. Cox, C.; Munk, W. Measurement of the Roughness of the Sea Surface from Photographs of the Sun's Glitter. *J. Opt. Soc. Am.* **1954**, *44*, 838–850. [CrossRef]
48. Available online: https://www.iso.org/standard/70908.html (accessed on 3 January 2026).
49. Taylor, R. Interpretation of the Correlation Coefficient: A Basic Review. *J. Diagn. Med. Sonogr.* **1990**, *6*, 35–39. [CrossRef]
50. Casal, G.; Harris, P.; Monteys, X.; Hedley, J.; Cahalane, C.; McCarthy, T. Understanding Satellite-Derived Bathymetry Using Sentinel 2 Imagery and Spatial Prediction Models. *GIScience Remote Sens.* **2020**, *57*, 271–286. [CrossRef]
51. Alikas, K.; Kratzer, S.; Reinart, A.; Kauer, T.; Paavel, B. Robust Remote Sensing Algorithms to Derive the Diffuse Attenuation Coefficient for Lakes and Coastal Waters. *Limnol. Oceanogr. Methods* **2015**, *13*, 402–415. [CrossRef]
52. Chen, L.; Zhang, J.; Pan, X.; Shi, P.; Zhang, X. Deriving the Vertical Variations in the Diffuse Attenuation Coefficient of Photosynthetically Available Radiation in the North Pacific Ocean from Remote Sensing. *Remote Sens.* **2023**, *15*, 3023. [CrossRef]

Disclaimer/Publisher's Note: The statements, opinions and data contained in all publications are solely those of the individual author(s) and contributor(s) and not of MDPI and/or the editor(s). MDPI and/or the editor(s) disclaim responsibility for any injury to people or property resulting from any ideas, methods, instructions or products referred to in the content.